Journal of the Geological Society, London, Vol. **162**, 2005, pp. 939–949. Printed in Great Britain.

Evolution of damage zone geometry and intensity in porous sandstone: insight gained from strain energy density

CHRIS. H. OKUBO* & RICHARD A. SCHULTZ

Geomechanics–Rock Fracture Group, Department of Geological Sciences and Engineering /172, Mackay School of Earth Sciences and Engineering, University of Nevada, Reno, NV 89557-0138, USA

**Present address: Lunar and Planetary Science Laboratory, University of Arizona, Tucson, AZ 85721, USA (e-mail: chriso@pirl.lpl.arizona.edu)*

Abstract: In porous geological materials such as sandstone or limestone, fault-related damage zones form arrays of deformation bands, which are planar discontinuities characterized by localized shear and porosity change. We show that the geometry and intensity of fault-related deformation band damage zones is systematic and predictable using standard strain energy density-based criteria. These criteria are used to successfully predict the tendencies for the nucleation and for the propagation of deformation bands as observed in a classic outcrop of fault-related damage zones within the brittly deformed Jurassic Wingate Sandstone exposed in the Laramide-aged Uncompahgre fold, in western Colorado, USA. The separate distributions of volumetric and distortional strain energy density are calculated for the interpreted geometry and stress state of the causative Laramide-aged thrust fault displacements from boundary element calculations of the attendant slip-induced local stresses. Volumetric strain energy density predicts the tendency for deformation band nucleation, the growth stage at which the deformation bands are defined by pore space dilatancy or collapse. Deformation band propagation, where shear occurs along the band, is predicted by distortional strain energy density. Further deformation bands at the Uncompahgre are predicted and observed to be characterized by shear-enhanced dilation.

Keywords: Wingate Sandstone, faulting, plastic deformation, sandstone, naturally fractured reservoirs.

A detailed mechanical understanding of the tendency for the nucleation and propagation of fault slip-induced secondary fractures is a key to evaluating the origins of fault-related damage zones and their effect on fault growth, stress transfer, and energy budget, as well as to evaluating the effect of brittle strain localization on the morphology, internal fracture structure, and fluid conductivity of fault-related folds. In this paper, we use numerical models of volumetric and distortional strain energy densities to successfully simulate independently observed geometries, intensities and propagation tendencies of deformation band damage zones around thrust faults within the Laramide-aged (Late Cretaceous to Mid-Eocene; *c*. 50–70 Ma old) Uncompahgre fold, in western Colorado, USA.

Geological background

Slip along a fault induces the nucleation and propagation of secondary damage zones within the surrounding rock. Because faults and their attendant damage zones can act as barriers (e.g. Jamison & Stearns 1982; Antonellini & Aydin 1994; Shipton *et al*. 2002; Sigda & Wilson 2003) or conduits (e.g. Sibson 1996; Campbell *et al*. 2003; Tripp & Vearncombe 2004) to fluid flow, the characterization of near-fault secondary fracturing is essential for evaluating the fluid flow, as well as seismic hazard, potential of fault-related folds. In this paper, we demonstrate how numerical model calculations of strain energy density can predict the distribution and intensity of near-fault secondary fractures within porous granular rock; specifically, the tendencies for nucleation and propagation of deformation bands within thrust fault-related folds. We use numerical models to predict the distribution of deformation band damage zones within the Jurassic Wingate Sandstone of the Laramide-aged Uncompahgre fold. As flexural slip folding is recognized as an important process in secondary fracture development within mechanically stratified fault-related folds (Roering *et al*. 1997; Cooke *et al*. 2000; Johnson & Johnson 2000), the distributions of deformation band damage zones are separately simulated for model fault geometries that allow for, and that prohibit, thrust-related flexural slip along the base of the Wingate Sandstone. Material strength and deformability parameters used to define the mechanical behaviour of the Wingate Sandstone are determined through new laboratory testing. We find that the model-predicted distributions and intensities of deformation band damage zones show convincing correlations with independent observations (Jamison & Stearns 1982) of deformation band damage zones within cross-sectional mode II exposures of the Uncompahgre fold and causative thrust faults.

Deformation bands

Deformation bands as defined in this paper are tabular localizations of plastic shear and porosity change within porous rock (Aydin 1978; Aydin & Johnson 1978) and can be the precursors to the nucleation of fully yielded fault surfaces (Aydin & Johnson 1983; Antonellini & Aydin 1994; Shipton & Cowie 2001; Schultz & Balasko 2003). Deformation bands have been referred to by various terminologies in reports of field observations and laboratory experiments of brittly deformed porous rock. They have been referred to as microfaults (Jamison & Stearns 1982), cataclastic slip bands (Du Bernard *et al*. 2002), braided shear fractures (Engelder 1974), granulation seams (Heald 1956; Pittman 1981) or band faults (Cruikshank *et al*. 1991, Zhao &

Johnson 1991). Deformation bands are distinct from Lüders' bands (Friedman & Logan 1973) or X shear bands (Crawford 1998), which are typically observed in laboratory compression tests of porous rock. Lüders' bands, or X shear bands, reflect diffuse compaction and shear deformation within the deformed laboratory sample and form because of the inhomogeneous stress state induced within the sample by typical laboratory setups (Olsson 2000) (rock core axially compressed between two steel platens, with or without lateral confining stress). Deformation bands form as a result of localized shear and pore volume change along a common yield plane and have been created in laboratory experiments where care has been taken to minimize inhomogeneous loading stresses within the test core (Mair *et al*. 2000, 2001).

The initial stage of natural or laboratory-induced deformation band nucleation is generally characterized by planar localizations of pore space collapse (Aydin 1978; Menéndez *et al*. 1996; Mair *et al*. 2001). With increasing strain, grain-scale shear displacements begin to occur along these planes of decreased porosity (Aydin 1978; Menéndez *et al*. 1996;Mair *et al*. 2000), and attendant shear-enhanced pore space compaction occurs under sufficient (rock-specific) magnitudes of mean stress, with dilation occurring at lesser values of mean stresses (Wong *et al*. 1997, 2004). These shear displacements may be accomplished through grain rolling, changes in packing geometry, and through grain crushing.

In this paper, the localization of pore space collapse prior to shearing is referred to as the nucleation stage of a deformation band. The subsequent accumulation of shear displacement across the deformation band is assumed to be contemporaneous with increases in band length (i.e. propagation) that are required to maintain a given shear displacement to band length ratio (Fossen & Hesthammer 1997; Schultz & Fossen 2002), which is a process common to faults and fractures (e.g. Cowie & Scholz 1992*a*, *b*). Accordingly, in terms of strain, deformation band nucleation is characterized by volumetric (normal) strain, whereas deformation band propagation is characterized by distortional (shear) strain.

Field observations of brittly deformed granular rock have shown that the extent and magnitude of fault-related damage zone strain is influenced by the distribution of fault slip. Measured deformation band intensities increase both normal to the fault plane (Jamison & Stearns 1982; Schultz & Fossen 2002) and ahead of and in-plane of the fault tip (Jamison & Stearns 1982). Deformation band intensity parallel to the plane of the fault also increases with the magnitude of fault displacement, leading to interpretations that fault slip promotes contemporaneous growth and widening of adjacent deformation band damage zones (Hesthammer *et al*. 2000; Shipton & Cowie 2001, 2003). Deformation band intensity also increases toward bedding plane faults related to flexural slip folding (Jamison & Stearns 1982), suggesting that mechanical stratification also influences damage zone growth.

The process of deformation band propagation can also lead to the nucleation of secondary deformation bands. Local stress concentration within compressive stepovers between two propagating echelon deformation bands is shown to induce the nucleation and propagation of secondary deformation bands (Schultz & Balasko 2003). With reference to Figure 1, secondary 'linking' deformation bands nucleate from one of the established 'bounding' bands and propagate toward and intersect the opposing 'bounding' band. Therefore deformation band propagation induces the nucleation of additional deformation bands in this distinct mode II compressive stepover geometry and thereby leads to an increase in the local deformation band intensity.

To predict the tendency for deformation band nucleation and propagation around a slipped thrust fault, we evaluate the distribution and magnitude of strain energy density, after Du & Aydin (1993) and Schultz & Balasko (2003). Du & Aydin (1993) used distortional strain energy density to create the first models of deformation band propagation in mode II that are consistent with field observations. Subsequently, Schultz & Balasko (2003)

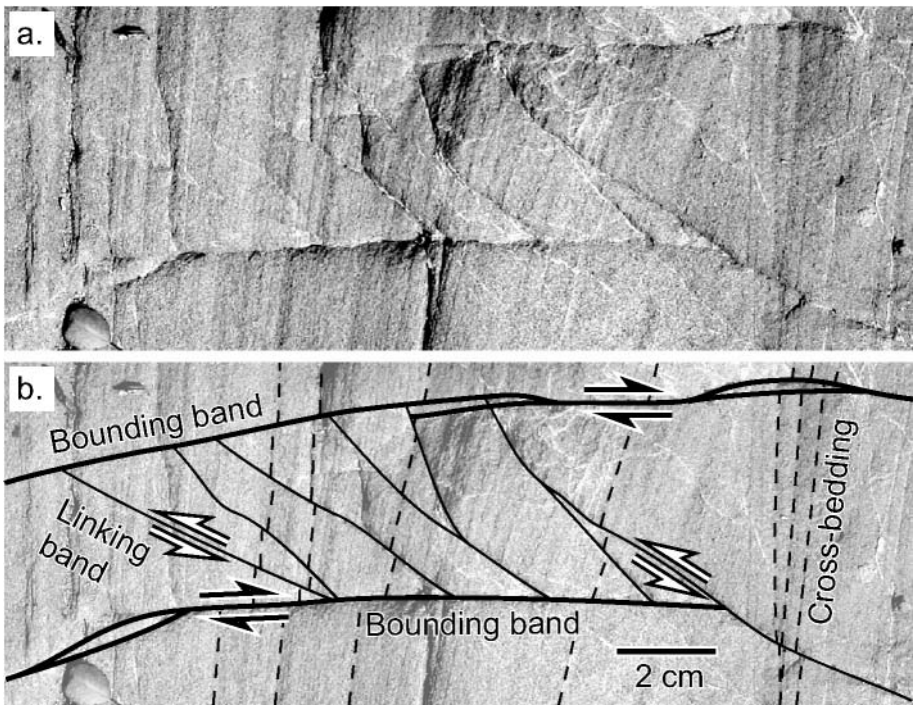

Fig. 1. Compressive mode II deformation band stepover structure in Wingate Sandstone from the area of Figure 3: (**a**) unannotated; (**b**) annotated photograph. Deformation bands are visible as thin white strands offsetting cross-beds (fine dashed lines). Accumulation of shear displacement and propagation of the two bounding bands (upper and lower bold lines) induces the nucleation and propagation of linking bands (fine continuous lines) between them (e.g. Schultz & Balasko 2003). Non-systematic deformation bands in (**b**) are unannotated for clarity.

used distortional strain energy density to successfully model the characteristic in-plane propagation of isolated deformation bands and to unravel the then enigmatic but widely observed compressive mode II deformation band stepovers (i.e. Fig. 1). Building upon this work, we incorporate numerical model calculations of volumetric strain energy density to predict the distribution of nucleating deformation bands. We also conduct laboratory testing to determine the critical strain energy density values at which deformation band nucleation and propagation will occur within the Wingate Sandstone. We then apply this analysis to the prediction of tens of metres-scale deformation band damage zones, whereas previous work focuses on the growth of single centimetre-scale bands.

Uncompahgre fold deformation bands

Exposures of kilometre-scale thrust faults coring the Laramide-aged Uncompahgre fold in Colorado National Monument, Colorado (Fig. 2) provide a superb opportunity to develop and test strain energy density-based predictions of deformation band damage zone growth. Details of the geological history of the Uncompahgre fold have been provided by numerous workers (e.g. Stone 1977; Scott *et al*. 2001), and a brief summary of the events relevant to this paper is presented here. Early growth of the Uncompahgre fold was driven by thrust displacement along pre-existing high-angle faults within a Precambrian metamorphic basement (migmatitic metasedimentary rocks) during the Late Carboniferous Period. Following cessation of fault slip, erosion during the Permian to Early Triassic Periods removed the pre-Late Carboniferous sedimentary cover and exposed the Precambrian basement of the fold. In the area of Colorado National Monument, this faulted basement was then blanketed by the interbedded mudstone, sandstone, conglomerate and limestone of the Chinle Formation during the remainder of the Triassic Period. Subsequently, aeolian sands of the Jurassic Wingate Sandstone were deposited, followed by the aeolian sands of the Kayenta Formation and Entrada Sandstone. Sedimentation continued until thrust displacements recurred along the Precambrian basement faults during the Laramide Orogeny (Late Cretaceous to Mid-Eocene). The thickness of the post-Carboniferous sedimentary cover at Colorado National Monument at the time of Laramide deformation is estimated to have been *c*. 1.8–2.1 km based on regional sedimentary exposures up through the Cretaceous Mancos Shale (Scott *et al*. 2001).

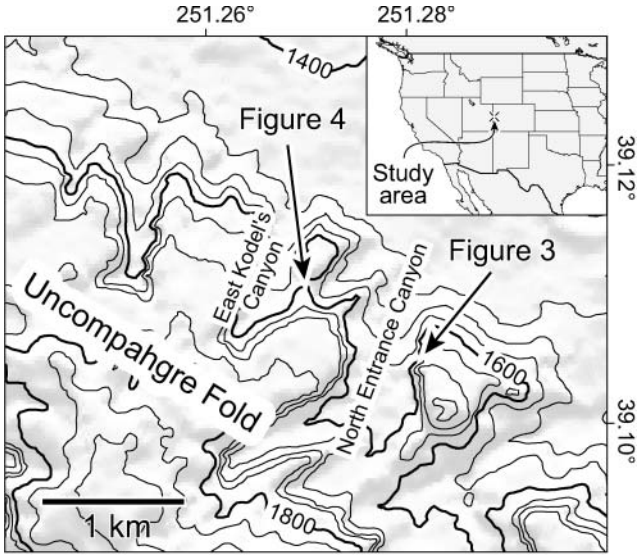

Fig. 2. Location map of the study area and key outcrops discussed in the text and figures. The Uncompahgre fold comprises the broad topographic highlands. Topographic contours are overlaid on shaded relief, with illumination from the north.

Within the Colorado National Monument, a network of canyons dissects the hinge of the Uncompahgre fold, exposing strata down to the faulted Precambrian basement. Exposures of Laramide-aged fault-related damage zones occur along the near-vertical walls of these canyons and provide clear evidence of the geometries and intensities of fault-related deformation band damage zones in mode II. This study focuses on the Laramide-aged growth of deformation band damage zones within the *c*. 100 m thick sequence of Jurassic Wingate Sandstone. The Wingate Sandstone is a fine-grained, very well-sorted aeolian deposit, with 20–24% porosity (Jamison & Stearns 1982), and contains *c*. 95% quartz with a light ferruginous cement (Stearns & Jamison 1977).

Stearns & Jamison (1977) and Jamison (1979) mapped the geometries and intensities of deformation band damage zones in cross-section around thrust faults exposed in North Entrance Canyon (Fig. 3) and East Kodel's Canyon (Fig. 4), within Colorado National Monument (Fig. 1). Early work by Stearns (1968), and subsequently Jamison (1989), showed that in these outcrops strain accommodated by deformation bands increases toward the fault. At low strains, deformation is accommodated by deformation band nucleation. Increasing strain results in increasing deformation band intensities, and in areas of higher

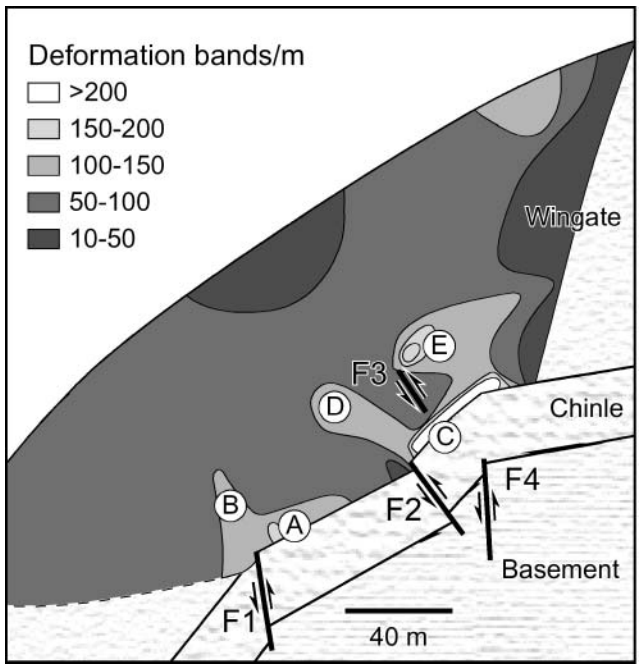

Fig. 3. Geometry and intensity of deformation band damage zones at North Entrance Canyon (see Fig. 2) as mapped in cross-section by Jamison & Stearns (1982). Within the Wingate Sandstone, deformation band intensity increases toward the solid white areas. Localizations of deformation bands are observed along the base of the Wingate Sandstone (points A and C) and adjacent to thrust faults (points B, D and E). Deformation band intensity in the damage zone at point E increases toward the upper tip of fault F3. Original Jamison & Stearns (1982) figure AAPG © 1982, reprinted by permission of the AAPG, whose permission is required for further use.

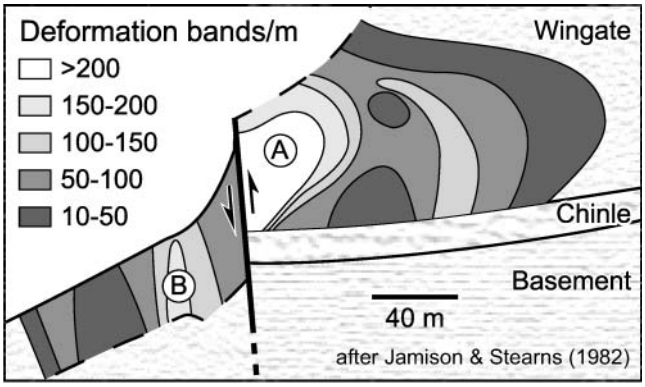

Fig. 4. Geometry and intensity of deformation band damage zones at East Kodel's Canyon (see Fig. 2) as mapped in cross-section by Jamison & Stearns (1982). Within the Wingate Sandstone, deformation band intensity increases toward the solid white areas. Deformation band intensity in the hanging-wall damage zone (point A) increases toward the plane of the fault. A smaller localization of deformation bands also occurs within the footwall at point B. Original Jamison & Stearns (1982) figure AAPG © 1982, reprinted by permission of the AAPG whose permission is required for further use.

strain, closer to the fault, deformation band intensity is shown to exceed 200 bands per metre. An exposure in East Kodel's Canyon is measured to have *c*. 10% horizontal strain owing to deformation band shear displacements, within a 0.9 m sampling domain (Jamison 1989). Together with this previous work, the exposures at the Uncompahgre fold provide clear standards for developing and testing numerical model predictions of the growth of deformation band damage zones.

The core of this paper will begin with a review of strain energy density. Next critical values for strain energy density, above which deformation band growth can be predicted, will be determined through laboratory testing of the Wingate Sandstone. Then, the paper will present systematic numerical model predictions of the cross-sectional distribution of strain energy density for the fault and fold geometries exposed in key outcrops in the Uncompahgre fold. The laboratory-derived critical strain energy density values will then be used to interpret regions of deformation band nucleation and propagation within the numerical model results. Finally, these predictions will be tested against the observed distribution of deformation band damage zones in the Uncompahgre exposures.

Critical strain energy densities for Wingate Sandstone

The amount of energy absorbed by normal and shear strain per unit volume can be quantified in terms of volumetric and distortional strain energy density, respectively. Equations for strain energy density are derived from the 3D forms of Hooke's Law for normal and shear stresses and strains, and are implicitly evaluated per unit volume. Volumetric strain energy density, S_v, is given by

$$S_v = \frac{1-2\nu}{6E}(\sigma_x + \sigma_y + \sigma_z)^2 \quad (1)$$

(Timoshenko & Goodier 1970, p. 247, equation (i)), and distortional (or deviatoric) strain energy density, S_d, is given by

$$S_d = \frac{1+\nu}{6E}[(\sigma_x - \sigma_y)^2 + (\sigma_y - \sigma_z)^2 + (\sigma_z - \sigma_x)^2] + \frac{1}{2G}(\tau_{xy}^2 + \tau_{xz}^2 + \tau_{yz}^2) \quad (2)$$

(Timoshenko & Goodier 1970, p. 248, equation (136)), where shear modulus, G, is

$$G = \frac{E}{2(1+\nu)}. \quad (3)$$

Therefore volumetric and distortional strain energy density can be readily calculated from stress state and standard measurements of material deformability (Young's modulus, E, and Poisson's ratio, ν). Calculation of strain energy densities in this paper are based on the compression positive sign convention. Signs of the volumetric and distortional strain energy densities are positive and independent of the sense of strain (dilational or compactive, left-lateral or right-lateral shear) because the signs of the causative stresses drop out of the governing equations (1) and (2).

Because deformation band nucleation is characterized by volumetric strain, volumetric strain energy density, S_v, can be used to assess the tendency for the nucleation of deformation bands around a slipped fault. Further, because deformation band propagation is associated with distortional strain, distortional strain energy density, S_d, can be used to assess the tendency for deformation band propagation. Deformation band nucleation and propagation (i.e. the onset of plastic yielding) can be predicted to occur at strain energy densities that are greater than critical values established through laboratory testing of the host rock.

To establish values of critical volumetric and distortional strain energy densities at the onset of deformation band growth within the Wingate Sandstone, we conduct a series of triaxial compression tests on Wingate Sandstone samples, as described in detail by Okubo & Schultz (in preparation). Blocks of Wingate Sandstone are obtained from the field, and test samples are prepared under controlled laboratory conditions following standard protocol for triaxial testing (ASTM International 1996). The final prepared Wingate Sandstone cores measure 11.6 cm in axial length and 5.3 cm in diameter (Fig. 5). Each core is then

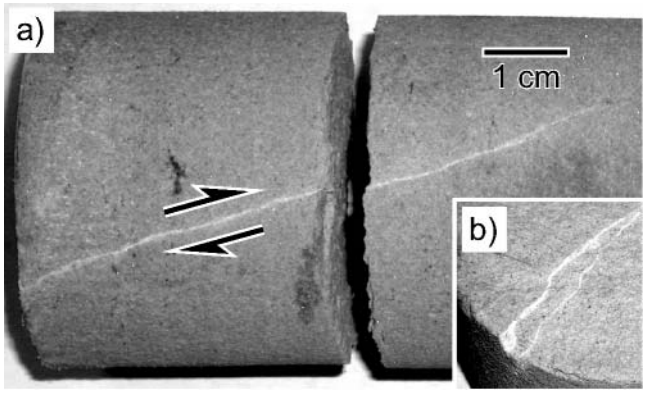

Fig. 5. Examples of deformation bands created by our laboratory tests. The deformation bands are visible as white strands (**a**) along the outer surface of the tested core and (**b**) in core cross-section. Sense of displacement is determined from offset cross-beds (core in (**a**) broke along a cross-bed upon extraction from the testing apparatus). Scale is the same in (**a**) and (**b**).

subjected to triaxial compression at prescribed confining pressures. Continuous measurements of axial and radial stress and strain are collected throughout the duration of each test and are used to monitor the transition from elastic to plastic strain. Figure 6 shows typical stress, strain and deformability relationships measured during each triaxial compression test. Stress is continuously applied at an axial strain rate of 1×10^{-4} s^{-1} during which time deformation bands nucleate and propagate. To gather data on the Coulomb strength of these bands, in a few tests (e.g. Fig. 6) stress is applied until the bands slip frictionally (e.g. Mair *et al*. 2000).

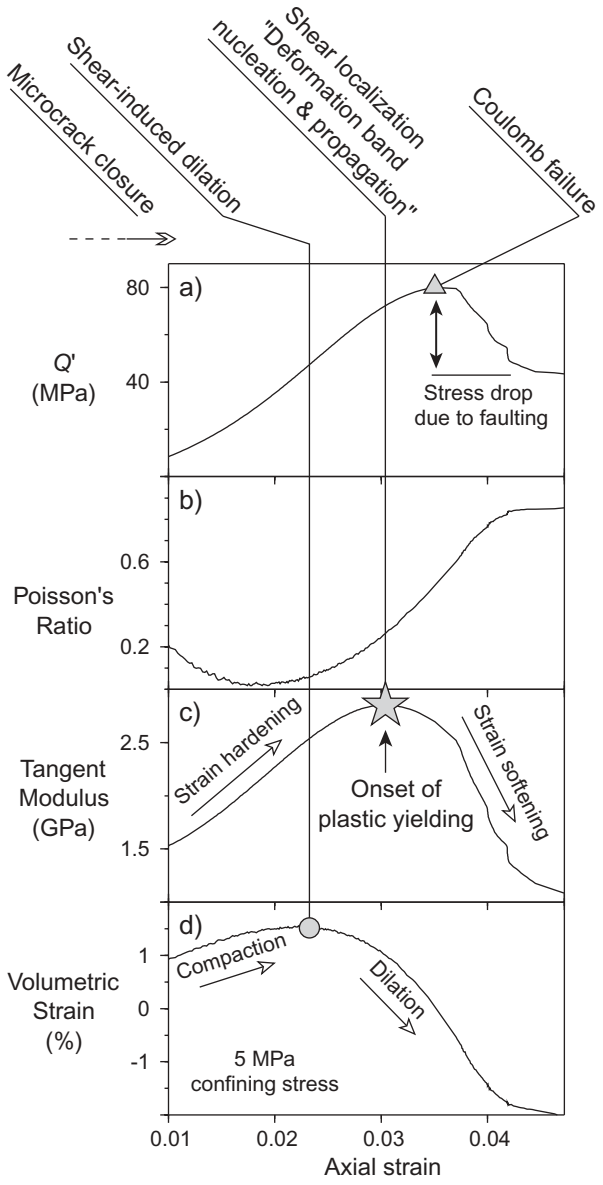

Fig. 6. Representative deformability curves from triaxial compression testing of Wingate Sandstone samples. The onset of plastic yielding, here deformation band nucleation and propagation, is marked by the maximum tangent modulus at *c*. 3% axial strain. This point also defines the critical stress state, P' (not shown), Q' and Poisson's ratio. Measurements of volumetric strain show that deformation band growth occurred through shear-enhanced dilation, consistent with microscopic observations of laboratory-deformed and naturally deformed Wingate Sandstone samples.

Visual inspection of the tested cores clearly shows brittle strain localization along individual deformation bands (Fig. 5). These bands are lighter-toned than the surrounding rock and show shear offsets of cross-bedding, consistent with observations of naturally formed deformation bands in Wingate Sandstone (Fig. 1). Further, photomicrograph analysis shows these laboratory-created deformation bands to be characterized by shear-enhanced dilation (increase in porosity toward the band), which is consistent with observations of naturally formed deformation bands at the Uncompahgre fold (Okubo & Schultz, in preparation).

The onset of plastic yielding in each test is defined as the point of maximum tangent modulus following (Vajdova *et al*. 2004; Wong *et al*. 2004). The stress states at plastic yield from each triaxial test cumulatively define the Wingate Sandstone's plastic yield function in terms of effective differential stress, Q', and effective mean stress, P'. The resulting best-fit yield envelope is defined by $Q'_{\text{yield}} = (-8.5 \times 10^{-4} \times P'^2) + (1.975 \times P')$, where plastic yielding is predicted for $Q' \geq Q'_{\text{yield}}$ at a given magnitude of P' (Okubo & Schultz, in preparation). This plastic yield function provides the magnitudes of the causative principal stresses, through Q' and P', at the onset of deformation band nucleation and propagation. Assuming average overburden densities of 2300–2600 kg m^{-3}, and a saturated ground water condition, yields lithostatic stress magnitudes of 22–28 MPa at the 1.7–1.8 km depth of the Wingate Sandstone during Laramide deformation at the Uncompahgre fold. Setting σ_3 equal to lithostatic stress yields causative σ_1 (most compressive horizontal stress) magnitudes of 146–186 MPa.

Values for the critical volumetric and distortional strain energy densities at the onset of deformation band nucleation and propagation are calculated from these causative principal stress magnitudes. Equations (1) and (2), for distortional and volumetric strain energy density, respectively, are solved using laboratory-defined values of E (4.9–7.0 GPa) and ν (0.17–0.19) for the critical stress state, with σx equal to σ_1 and σy equal to σ_2. σz is thus the intermediate compressive stress and is calculated as

$$\sigma_z = \nu(\sigma_x + \sigma_y). \tag{4}$$

The critical values of S_v for deformation band nucleation are found to be 0.86–1.0 MJ m^{-3}, and the critical values of S_d for deformation band propagation are 1.14–1.3 MJ m^{-3}. Therefore deformation band nucleation and propagation within the Wingate Sandstone during Laramide deformation at the Uncompahgre fold are predicted where magnitudes of strain energy density equal or exceed these critical values.

Numerical prediction of deformation band growth

A series of numerical models are next created to predict the magnitudes and distributions of distortional and volumetric strain energy density for comparison with the field observations of deformation band distribution and intensity reported by Jamison & Stearns (1982). The goal of this analysis is to test the applicability of strain energy density for predicting deformation band damage zone geometries around a slipped fault. We use the 2D boundary element code FAULT (Schultz 1992) to simulate the distribution of stresses around a slipped thrust fault within a linear elastic half-space.

The numerical models are designed to simulate the distribution of stresses around a Laramide-aged basement-involved thrust fault, allowing for different upper tip depths and either a welded or a non-welded contact at the base of the Wingate Sandstone. In

our numerical models, the Precambrian basement and overlying sedimentary units are each idealized as a mechanically homogeneous rock mass. The Chinle Formation is first modelled as a part of the greater homogeneous rock mass to simulate a mechanically welded contact between the Wingate Sandstone and Precambrian basement. The Chinle Formation is then modelled as a deformable contact that is permitted to slip under a Coulomb frictional slip criteria. Modelling the Chinle Formation as a frictionally slipping contact allows for an evaluation of the effect of flexural slip folding on the predicted distribution of strain energy densities and deformation band damage zones within the Wingate Sandstone. In line with interpretations of regional stratigraphy at the time of Laramide deformation (Scott *et al*. 2001), the model Wingate Sandstone is placed at 1.7–1.8 km depth, the contact with the Chinle Formation is placed at 1.8 km depth, and the Precambrian basement is below 1.8 km depth.

For both scenarios of a mechanically welded and a frictionally slipping Chinle Formation, the depth of the upper fault tip is varied, to predict the distribution of strain energy density corresponding to the thrust fault geometries described by Jamison & Stearns (1982) (Figs 3 and 4). The upper tip of the model thrust fault is prescribed to terminate at 50 m below the Chinle Formation (within the Precambrian basement), then at the Chinle Formation, and finally at the mid-depth of the Wingate Sandstone. These three upper tip depths are used in conjunction with the mechanically welded and frictionally slipping Chinle Formation scenarios, resulting in six model configurations. The lower tip of the model thrust fault is kept at a constant depth of 10 km in all model scenarios, and the model thrust has a listric geometry (Fig. 7).

The causative plane strain stress state prescribed in our models is based on the interpreted stratigraphy at the time of Laramide deformation and the laboratory-derived strength of the Wingate Sandstone. Assuming an Andersonian stress state for thrust faulting (Anderson 1951), σ_3 is vertical and corresponds to lithostatic load, and σ_1 acts in the horizontal direction. Assuming an average density of 2450 kg m^{-3} for the overlying sedimentary units and saturated groundwater conditions, the depth-dependent σ_3 gradient is therefore 15 MPa km^{-1}. Our laboratory analyses show that the principal stress ratio at the onset of plastic yielding in the Wingate Sandstone is *c*. 6.6 at this range of σ_3. Therefore the depth-dependent σ_1 gradient is prescribed to be 99 MPa km^{-1}. Additionally, the model rock mass has a uniform Young's modulus of 6.0 GPa and Poisson's ratio of 0.19, in line with laboratory test results.

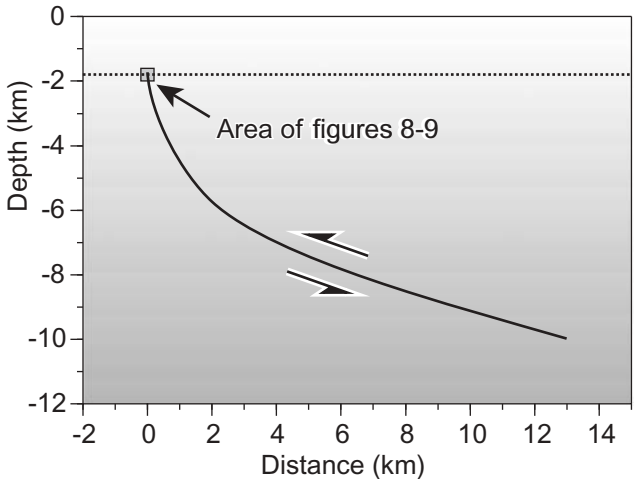

Fig. 7. Geometry of frictionally slipping thrust fault elements (continuous curved line) and bedding-plane elements (dotted horizontal line) modelled in the FAULT boundary element code. Numerical model predictions of strain energy density are shown in Figures 8 and 9 for the region surrounding the upper fault tip. Sense and distribution of slip along the model fault and bedding-plane elements is driven by the prescribed stress state and strength and deformability parameters.

The distribution of slip along the model thrust fault is calculated in FAULT as a function of the resolved stresses acting along each fault plane element. The tendency for slip along each fault element is evaluated using the local stress form of the Coulomb failure criterion. Slip occurs along fault elements where the combined magnitudes of the frictional and cohesive resisting strengths are less than the absolute magnitude of the resolved shear stress acting along that element. Then for each frictionally slipping fault element, the amount of accommodated displacement is calculated from the prescribed shear modulus of the surrounding rock mass and the magnitude of the resolved shear stress. Additionally, the displacements and stresses within the surrounding matrix (rock mass) owing to fault slip are calculated by assuming linear elastic half-space conditions. These fault slip-induced stresses within the surrounding matrix are then used to calculate values of strain energy density using equations (1)–(4).

Results

Mechanically welded contact

The predicted distribution of strain energy density in the case where the Wingate Sandstone and Chinle Formation are mechanically welded to the faulted Precambrian basement are shown in Figure 8. Areas with predicted strain energy densities above the mean critical values for S_v of 0.93 MJ m^{-3} and S_d of 0.93 MJ m^{-3} are shaded in greyscale, with increasing values toward white. At all modelled upper tip depths, large magnitudes of volumetric strain energy density are predicted adjacent to the upper fault tip, within the upper hanging wall (e.g. Fig. 8a, point P). Conversely, the magnitude of volumetric strain energy density decreases toward the footwall and falls below the critical density for deformation band nucleation (e.g. Fig. 8a, point Q). Large magnitudes of distortional strain energy density are localized in an elongate lobe ahead of the fault tip (e.g. Fig. 8b, point R), as well as in smaller lobes immediately behind the upper fault tip in both the hanging wall (e.g. Fig. 8b, point S) and footwall (e.g. Fig. 8b, point T). At the three modelled upper tip depths, the magnitude of predicted distortional strain energy density remains greater than the critical value.

These model predictions lead to distinct geometries for zones of nucleating deformation bands adjacent to a slipped fault, in the absence of fault-related folding (slip along the base of the Wingate Sandstone). Volumetric strain energy densities greater than the critical value are assumed to be associated with enhanced deformation band nucleation tendency. Thus zones of nucleating deformation bands are expected to follow the model-predicted patterns of high volumetric strain energy densities. Analysis of Figure 8 therefore predicts zones of nucleating deformation bands within the upper hanging wall of the thrust (e.g. Fig. 8a, point P). This zone of nucleating deformation bands is elongate parallel to the down-dip trace of the fault. Further, deformation band intensity is predicted to increase toward and ahead of the upper fault tip, following the higher volumetric strain energy densities in those areas.

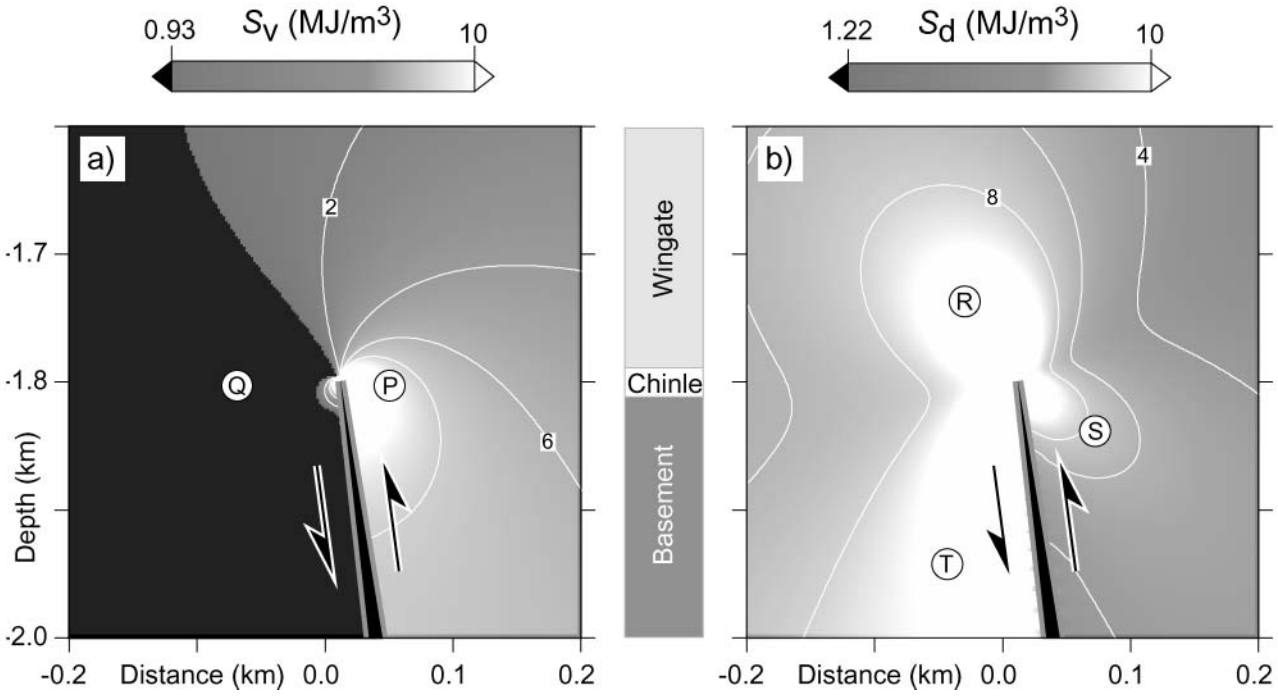

Fig. 8. Numerical model predictions of the distribution and magnitudes of (**a**) volumetric and (**b**) distortional strain energy density where frictional slip does not occur along the Chinle Formation interface between the Wingate Sandstone and Precambrian basement. A lobe of high volumetric strain energy density (enhanced deformation band nucleation tendency) is predicted within the hanging wall of the thrust in (**a**), whereas lobes of high distortional strain energy densities (enhanced deformation band propagation tendencies) are predicted around and ahead of the upper fault tip in (**b**). Variations of ±100 m in the depth of the upper tip have negligible effect on the results shown here; the high-density lobes track the relative position of the upper tip. Locations of labelled points are referred to in the discussion.

Additionally, analysis of the model-predicted distributions of distortional strain energy density in Figure 8a and b reveals lobes of enhanced deformation band propagation around the thrust fault in the absence of fault-related folding. These lobes of enhanced propagation tendency overlap the regions of enhanced nucleation tendency. Thus deformation bands that nucleated during a previous slip event, or earlier during the same slip event, will be subjected to an enhanced tendency for propagation within these lobes. An elongate lobe of enhanced propagation is located ahead of the upper fault tip (e.g. Fig. 8b, point R), accompanied by an elongate lobe within the upper footwall (e.g. Fig. 8b, point T) and a smaller lobe within the upper hanging wall (e.g. Fig. 8b, point S). The tendency for deformation band propagation will be greatest ahead of the upper tip of the fault and within the upper hanging wall and footwall adjacent to the upper fault tip. Deformation band propagation may also occur adjacent to the fault plane away from the upper tip, with the greatest propagation tendencies closest to the fault plane.

Frictionally slipping contact

In the next set of models, the Chinle Formation is modelled as a frictionally slipping contact between the Wingate Sandstone and faulted basement (Fig. 9). Where the upper fault tip is below the Wingate Sandstone, fault-induced frictional slip along the Chinle Formation induces a localization of elevated volumetric strain energy density along the base of the Wingate Sandstone above the upper hanging wall of the thrust (Fig. 9a, point P). This localization increases in size and magnitude when the upper tip of the thrust intersects the Chinle Formation (Fig. 9b, point Q). Finally, where the upper tip of the thrust is within the Wingate Sandstone, a lobe of high volumetric strain energy density occurs within the upper hanging wall of that thrust, with the greatest magnitudes of strain energy density near the upper fault tip (Fig. 9c, point R). This lobe is elongate away from the upper tip, within the upper hanging wall, and merges into the elevated volumetric strain energy densities along the base of the Wingate Sandstone (Fig. 9c, point S).

Additionally, elevated values of distortional strain energy density are also predicted to localize along the base of the Wingate Sandstone when this interface is modelled as a frictional contact that is slipping in response to fault-related folding. Where the upper fault tip is below the base of the Wingate Sandstone, within the faulted basement, a localization of high distortional strain energy density occurs along the base of the Wingate Sandstone (Fig. 9d, point T) and ahead of the up-dip projection of the thrust within the Wingate Sandstone (point U). Next, where the upper thrust tip intersects the Chinle Formation, the localizations of distortional strain energy density along the base of the Wingate Sandstone (Fig. 9e, point V) and ahead of the fault tip (point W) increase in magnitude. Finally, where the upper thrust tip is within the Wingate Sandstone, a lobe of high distortional strain energy density is predicted elongate ahead of and slightly within the footwall of the thrust (Fig. 9f, point X), with the magnitude of strain energy density increasing toward the upper fault tip. Other lobes of elevated strain energy density also occur within the upper hanging wall (point Y) and footwall (point Z) of the thrust. The lobe within the upper hanging wall is elongate away from the upper thrust tip, into the upper hanging wall, and again the magnitude of strain energy density increases

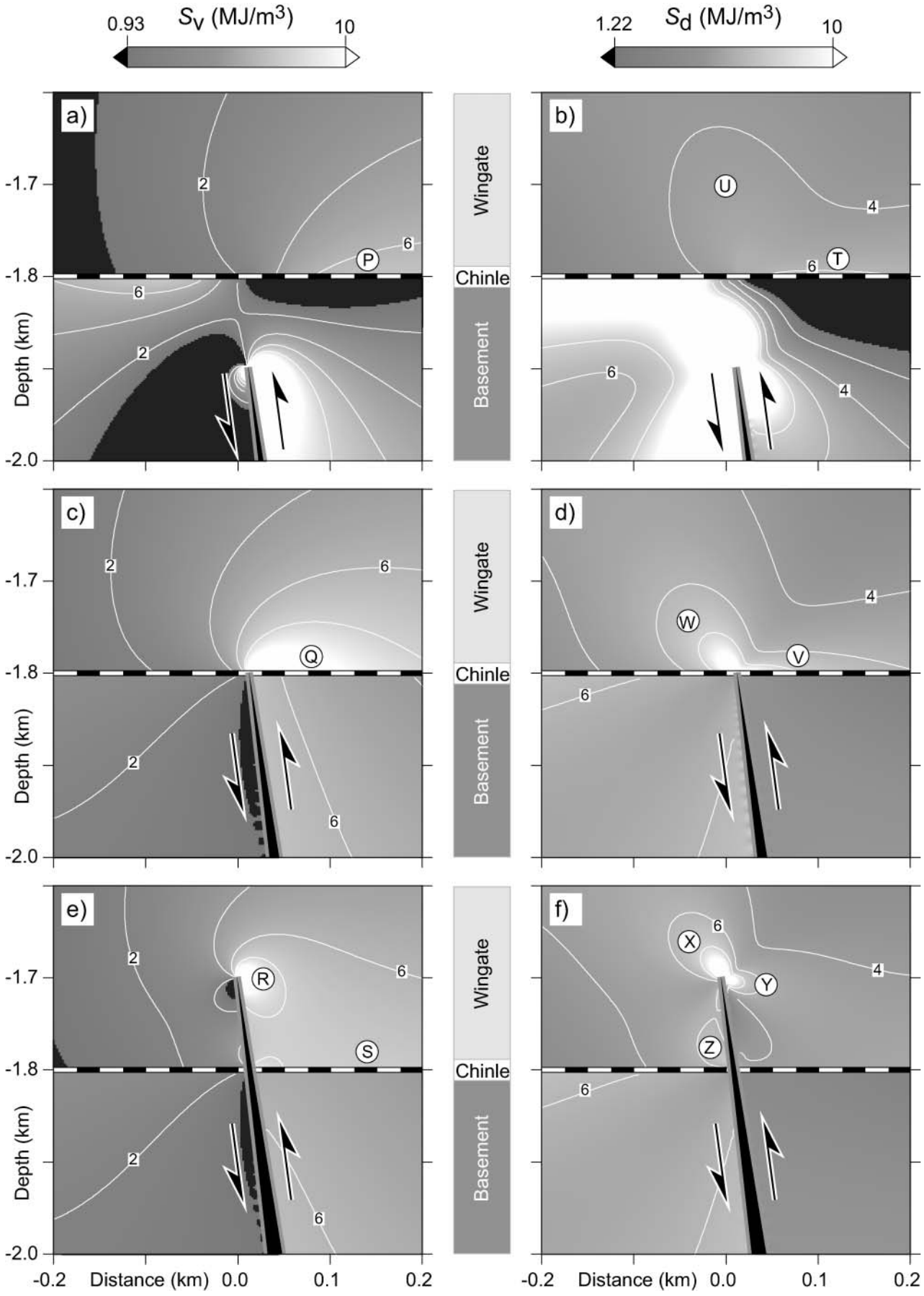
0.93 S_V (MJ/m^3) 10
1.22 S_d (MJ/m^3) 10
a)
b)
c)
d)
e)
f)
Wingate
Chinle
Basement
Depth (km)
-1.7
-1.8
-2.0
Distance (km)
-0.2
0.0
0.1
0.2
2
4
6
P
Q
R
S
T
U
V
W
X
Y
Z

toward the upper tip of the thrust. The lobe within the upper footwall is elongate subparallel to the plane of the thrust, and strain energy densities increase in proximity to the fault plane.

Analysis of Figure 9 shows that deformation bands are predicted to preferentially nucleate above a frictionally slipping contact (points P, Q and S). The tendency for nucleation above the slipping contact is greatest where the upper tip of the thrust intersects the base of the Wingate Sandstone. Where the upper tip of the thrust is within the Wingate Sandstone, high deformation band intensities are predicted in a zone that is elongate away from the upper fault tip within the hanging wall (point R), with the highest intensities in this lobe located toward the fault tip.

The locations and geometries of lobes of enhanced deformation band propagation tendency are also predicted to be affected by frictional slip along the base of the Wingate Sandstone. Where the upper tip of the thrust is below the base of the Wingate Sandstone, deformation band propagation tendency is highest along the base of the Wingate Sandstone above the hanging wall of the thrust (Fig. 9d, point T) and ahead of the upper tip of the thrust (point U). These tendencies increase in magnitude where the upper tip of the thrust intersects the base of the Wingate Sandstone (points V and W). Where the upper thrust tip is within the Wingate Sandstone, the tendency for deformation band propagation is enhanced ahead of the fault tip and slightly within the upper footwall (Fig. 9f, point X). Further, the tendency for propagation is also enhanced within the upper hanging wall (Fig. 9f, point Y) and within the upper footwall adjacent to the fault plane (point Z).

Comparison of Figures 8 and 9 shows that frictional slip along the base of the Wingate Sandstone is predicted to significantly and characteristically affect the resulting geometries and intensities of deformation band damage zones. The predicted localization of damage zones along the base of the Wingate Sandstone is shown to be an especially distinct result of frictional slip along that contact. Also, because the predicted magnitudes of distortional and volumetric strain energy density are nearly everywhere above the respective critical values, these deformation band damage zones are also expected to occur within, and be distinct from, a background level of nucleating and propagating deformation bands.

Discussion

Our strain energy density-based predictions of damage zone geometries and intensities around slipped thrust faults, for the scenario where flexural slip folding occurs along the base of the Wingate Sandstone (Fig. 9), show compelling consistencies with the geometries and intensities of the deformation band damage zones mapped by Jamison & Stearns (1982) within the Uncompahgre fold (Figs 3 and 4). Also as our models predict, the observed deformation band damage zones occur within, and are distinct from, a background intensity of deformation bands. Based on these comparisons, we can now make some interpretations of the origins and maturity of the observed deformation band damage zones.

At the North Entrance Canyon outcrop, a thrust fault we provisionally identify as F1 (Fig. 3) intersects the base of the Wingate Sandstone. Here, the damage zone is marked by elevated deformation band densities along the base of the Wingate Sandstone above the hanging wall of the thrust (point A). This damage zone geometry is consistent with the characteristic geometry predicted for a damage zone of nucleating deformation bands growing above a frictionally slipping contact (Fig. 9b, point Q). Therefore, we propose that the deformation band damage zone of Figure 3, point A, consists predominantly of nucleating deformation bands and is a result of frictional slip along the base of the Wingate Sandstone induced by slip along fault F1 as it impinged upon the base of the Wingate Sandstone. The interpretation that these deformation bands have only nucleated but not propagated suggests that these bands are relatively short and thin (not having propagated).

Also at fault F1, a damage zone is observed ahead of and slightly above the footwall of the fault plane (Fig. 3, point B). This geometry is strikingly similar to the predicted damage zone geometry for propagating deformation bands above a thrust tip that intersects the base of the Wingate Sandstone (Fig. 9e, point W). Based on this similarity, we propose that the damage zone in Figure 3, point B, primarily consists of deformation bands that have accumulated shear and propagated in response to slip along fault F1, as it impinged upon the base of the Wingate Sandstone. Interpretation that these deformation bands have propagated suggests that they are relatively longer, thicker and more interconnected than the bands in the damage zone of point A, which have only nucleated. Thus the degree of porosity and permeability reduction is expected to be greater, and fluid conductivity may be significantly more reduced, in this damage zone (point B) compared with in the damage zone of point A.

Similar interpretations can be made for the deformation band damage zone of fault F2, where elevated deformation band intensities are observed along the base of the Wingate Sandstone (Fig. 3, point C) and ahead of the upper tip above the footwall (Fig. 3, point D). In contrast to the damage zone of fault F1, the damage zone along the base of the Wingate Sandstone for fault A2 shows higher deformation band densities ($>200\ m^{-1}$ vs. between 100 and $200\ m^{-1}$). This may reflect higher volumetric strain energy densities along the base of the Wingate Sandstone (e.g. Fig. 9b, point Q), which have led to a greater enhancement of deformation band nucleation tendency here. Relatively larger volumetric strain energy densities here may be the result of higher near-tip stresses. Potential sources of elevated near-tip stress at fault F2 may include a larger near-tip displacement gradient along fault F2, a greater cumulative displacement along F2, or displacement and stress interaction with adjacent faults such as F3 or F4.

The elongate damage zone of fault F3 (Fig. 3, point E) is strongly consistent with the damage zone geometry and deformation band intensity distribution predicted for a zone of nucleating deformation bands adjacent to the upper tip of a thrust fault in the presence of fault-related flexural slip folding, where the upper tip is within the Wingate Sandstone (Fig. 9c, point R). The

Fig. 9. Numerical model predictions of the distribution and magnitudes of volumetric (**a**, **c**, **e**) and distortional (**b**, **d**, **f**) strain energy densities where frictional slip occurs along the Chinle Formation interface between the Wingate Sandstone and Precambrian basement. Lobes of high volumetric strain energy density (enhanced deformation band nucleation tendency) are predicted within the hanging walls of the thrust in (**a**), (**c**), and (**e**), whereas lobes of high distortional strain energy density (enhanced deformation band propagation tendencies) are predicted around and ahead of the upper fault tips in (**b**), (**d**), and (**f**). Thrust-induced frictional slip along the Chinle Formation is shown to significantly influence the distributions of the high-density lobes. Locations of labelled points are referred to in the discussion.

predicted and observed damage zones are elongate away from the upper tip of the fault and within the upper hanging wall. Also, deformation band intensity within the damage zone increases toward the upper fault tip. Therefore the damage zone of Figure 3, point E, is predicted to consist primarily of deformation bands that have only nucleated, forming in response to the propagation of fault F3 into the Wingate Sandstone.

Our predictions of distinct nucleation-dominant and propagation-dominant deformation band damage zones are an important step in understanding the potential distribution of reduced fluid conductivity around faults in porous granular rock as a result of damage zone growth. These predictions can be tested by comparing the predicted distribution of propagation-dominant damage zones against the distribution of compressive mode II deformation band stepover structures (i.e. Fig. 1) mapped by Jamison & Stearns (1982) at this outcrop. As these stepover structures form only between two propagating deformation bands, the damage zones that we predict to be propagation-dominant should contain these stepover structures, whereas these stepover structures should be absent from the damage zones that we predict to be nucleation-dominant.

Jamison & Stearns (1982) mapped localizations of mode II stepover structures ahead of the upper tips of faults F1 and F2, at the location of points B and D in Figure 3. These locations correspond to the damage zones where our numerical models predict elevated distortional strain energy densities and where we predict enhanced tendencies for deformation band propagation. Also, at the damage zone of fault F3 where we predict dominant deformation band nucleation tendencies (Fig. 3, point E), mode II stepover structures are not observed, consistent with the predicted predominance of nucleation processes here. Additionally, mode II stepover structures are not observed within the damage zones along the base of the Wingate Sandstone, where we predict nucleation to be the dominant deformation band process (Fig. 3, points A and C). Therefore we find that our predictions of nucleation-dominant and propagation-dominant damage zones are confirmed by independent field observations.

Jamison & Stearns (1982) also mapped thrust fault related deformation band damage zones at their East Kodel's Canyon site (Fig. 4), where the Wingate Sandstone is completely transected by a single thrust fault. The deformation band damage zone is most prominent within the hanging wall of the thrust, and deformation band intensity is observed to increase toward the intersection of the thrust and the base of the Wingate Sandstone (Fig. 4, point A). A smaller and lower intensity damage zone also occurs within the footwall of the thrust (Fig. 4, point B). We interpret these deformation band damage zones as relict structures related to an earlier stage of fault growth, when the upper tip of the thrust was near the mid-depth or base of the Wingate Sandstone. In this previous fault geometry, deformation bands are predicted to have high nucleation tendencies within a lobe above the upper tip and within the hanging wall of the thrust (Fig. 4, point A), as interpreted from the elevated volumetric strain energy densities predicted in Figure 9b, point Q, and Figure 9c, point R. Further, the slightly elevated deformation band densities in the footwall (Fig. 4, point B) can be attributed to deformation band propagation as a result of elevated distortional strain energy densities when the upper tip was between the mid-depth and base of the Wingate Sandstone (i.e. Fig. 9e, point W, or Fig. 9f, points X and Z). These predicted tendencies are consistent with the distribution of compressive mode II stepover structures mapped by Jamison & Stearns (1982). Stepover structures are observed within the footwall damage zone, where we predict deformation band propagation, and stepover structures are absent from the hanging-wall damage zone, where we predict predominantly deformation band nucleation.

The strong correlation between model predictions and independent field observations provides significant confidence in the reliability of the proposed strain energy density criteria for predicting the distribution and intensity of deformation band damage zones. Our model-predicted deformation band intensities, damage zone geometries, and predominant growth mode distribution (nucleation vs. propagation) are consistent with the field observations made by Jamison & Stearns (1982). We find no anti-correlation between our model predictions and their field observations.

Summary and implications

Based on comparisons with independent field observations of fault-related deformation band damage zones, we find that the geometry and intensity of deformation band damage zones, and the tendency for deformation band nucleation and propagation within these zones, as well as the nature of porosity change across the bands (dilation vs. compaction), are systematic and predictable based on laboratory testing and numerical models of the distribution of fault-induced strain energy density within the surrounding fold. Within each damage zone, the separate tendencies for deformation band nucleation and for propagation are predictable from separate calculations of volumetric and distortional strain energy density, respectively.

The method used here to predict the distribution, intensity and maturity of deformation band damage zones can be a powerful tool for future applications because of the flexibility of the required input parameters. Our numerical model setup is based on observations and measurements of fault geometry and material strength within the Uncompahgre fold. Alternatively, where fault geometry is not known, or even where a fault is not present, a numerical model inversion of fold topography can be used to predict the distribution of the attendant stresses and strain energy densities. Additionally, the effects of spatial and temporal variability or uncertainty in material strength and deformability, groundwater condition, fault geometry, or stress state can be readily investigated using appropriate variations of a common model.

Although this method shows great potential for predicting deformation band damage zone geometries, care must be exercised in extrapolating our predictions to other natural systems. Most importantly, our models assume that the Wingate Sandstone is initially homogeneous, lacking pervasive pre-existing fractures or other mechanical discontinuities. Therefore the resulting predictions of deformation band damage zone geometry, intensity and maturity are most applicable to a mechanically homogeneous non-fractured host rock. This pristine fracture condition for the Wingate Sandstone is based on our observations and those of Jamison & Stearns (1982) that mode I fractures at their field sites are few in number, relative to the deformation band population, and that cross-cutting relations indicate that many of these mode I fractures are younger than the deformation bands. In other natural systems, the presence of pervasive pre-existing fractures or other mechanical discontinuities within the host rock may significantly affect deformation band growth processes and result in damage zone geometries, intensities, and nucleation and propagation tendencies that diverge from our predictions.

This work is supported by NASA's Planetary Geology and Geophysics Program. We thank J. Evans and I. Main for constructive reviews of the

manuscript. Laboratory testing was made possible by R. Blitz, J. Daemen, and D. van Zyl. Thanks go to R. Baden of Grafix Plastics for providing Melinex, and to R. Soliva and P. Eeps for help in obtaining samples of Wingate Sandstone. We also thank G. Stefanelli of the W. M. Keck Earth Sciences and Mining Research Information Center for providing computing support.

References

Anderson, E.M. 1951. *The Dynamics of Faulting and Dyke Formation, with Applications to Britain*. Oliver & Boyd, Edinburgh.

Antonellini, M. & Aydin, A. 1994. Effect of faulting on fluid flow in porous sandstones; petrophysical properties. *AAPG Bulletin*, **78**, 355–377.

ASTM International 1996. Practice for preparing rock core specimens and determining dimensional and shape tolerances. *Annual Book of ASTM Standards*, **4**, D4543.

Aydin, A. 1978. Small faults formed as deformation bands in sandstone. *Pure and Applied Geophysics*, **116**, 913–930.

Aydin, A. & Johnson, A.M. 1978. Development of faults as zones of deformation bands and as slip surfaces in sandstone. *Pure and Applied Geophysics*, **116**, 931–942.

Aydin, A. & Johnson, A.M. 1983. Analysis of faulting in porous sandstones. *Journal of Structural Geology*, **5**, 19–31.

Campbell, K., Wolfsberg, A., Fabryka-Martin, J. & Sweetkind, D. 2003. Chlorine-36 data at Yucca Mountain: statistical tests of conceptual models for unsaturated-zone flow. *Journal of Contaminant Geology*, **62-63**, 143–161.

Cooke, M.L., Mollema, P.N., Pollard, D.D. & Aydin, A. 2000. Interlayer slip and joint localization in the East Kaibab Monocline, Utah: field evidence and results from numerical modeling. *In:* Cosgrove, J.W. & Ameen, M.S. (eds) *Forced Folds and Fractures*. Geological Society, London, Special Publications, **169**, 23–49.

Cowie, P.A. & Scholz, C.H. 1992a. Physical explanation for the displacement–length relationship of faults using a post-yield fracture mechanics model. *Journal of Structural Geology*, **14**, 1133–1148.

Cowie, P.A. & Scholz, C.H. 1992b. Displacement–length scaling relationship for faults; data synthesis and discussion. *Journal of Structural Geology*, **14**, 1149–1156.

Crawford, B.R. 1998. Experimental fault sealing; shear band permeability dependency on cataclastic fault gouge characteristics. *In:* Coward, M.P., Daltaban, T.S. & Johnson, H. (eds) *Structural Geology in Reservoir Characterization*. Geological Society, London, Special Publications, **127**, 27–47.

Cruikshank, K.M., Zhao, G. & Johnson, A.M. 1991. Duplex structures connecting fault segments in Entrada sandstone. *Journal of Structural Geology*, **13**, 1185–1196.

Du, Y. & Aydin, A. 1993. The maximum distortional strain energy density criterion for shear fracture propagation with applications to the growth paths of en echelon faults. *Geophysical Research Letters*, **20**, 1091–1094.

Du Bernard, X., Labaume, P., Darcel, C., Davy, P. & Bour, O. 2002. Cataclastic slip band distribution in normal fault damage zones, Nubian sandstones, Suez rift. *Journal of Geophysical Research*, **107**, 2141.

Engelder, J.T. 1974. Cataclasis and the generation of fault gouge. *Geological Society of America Bulletin*, **85**, 1515–1522.

Fossen, H. & Hesthammer, J. 1997. Geometric analysis and scaling relations of deformation bands in porous sandstone. *Journal of Structural Geology*, **19**, 1479–1493.

Friedman, M. & Logan, J.M. 1973. Lüders' bands in experimentally deformed sandstone and limestone. *Geological Society of America Bulletin*, **84**, 1465–1476.

Heald, M.T. 1956. Cementation of Simpson and St. Peter Sandstone in parts of Oklahoma, Arkansas, and Missouri. *Journal of Geology*, **64**, 16–30.

Hesthammer, J., Johansen, T.E.S. & Watts, L. 2000. Spatial relationships within fault damage zones in sandstone. *Marine and Petroleum Geology*, **17**, 873–893.

Jamison, W.R. 1979. *Laramide deformation of the Wingate Sandstone, Colorado National Monument: a study of cataclastic flow*. PhD dissertation, Texas A&M University, College Station, TX.

Jamison, W.R. 1989. Fault-fracture strain in Wingate Sandstone. *Journal of Structural Geology*, **11**, 959–974.

Jamison, W.R. & Stearns, D.W. 1982. Tectonic deformation of Wingate Sandstone, Colorado National Monument. *AAPG Bulletin*, **66**, 2584–2608.

Johnson, K.M. & Johnson, A.M. 2000. Localization of layer-parallel faults in San Rafael swell, Utah and other monoclinal folds. *Journal of Structural Geology*, **22**, 1455–1468.

Mair, K., Main, I. & Elphick, S. 2000. Sequential growth of deformation bands in the laboratory. *Journal of Structural Geology*, **22**, 25–42.

Mair, K., Elphick, S. & Main, I. 2001. Influence of confining pressure on the mechanical and structural evolution of laboratory deformation bands. *Geophysical Research Letters*, **29**, 1410.

Menéndez, B., Zhu, W. & Wong, T.-f. 1996. Micromechanics of brittle faulting and cataclastic flow in Brea sandstone. *Journal of Structural. Geology*, **18**, 1–16.

Olsson, W.A. 2000. Origin of Lüders' bands in deformed rock. *Journal of Geophysical Research*, **105**, 5931–5938.

Pittman, E.D. 1981. Effect of fault related granulation on porosity and permeability of quartz sandstones, Simpson Group (Ordovician), Oklahoma. *AAPG Bulletin*, **65**, 2381–2387.

Roering, J.J., Cooke, M.L. & Pollard, D.D. 1997. Why blind thrust faults do not propagate to the Earth's surface: numerical modeling of coseismic deformation associated with thrust-related monoclines. *Journal of Geophysical Research*, **102**, 11902–11912.

Schultz, R.A. 1992. Mechanics of curved slip surfaces in rock. *Engineering Analysis with Boundary Elements*, **10**, 147–154.

Schultz, R.A. & Balasko, C.M. 2003. Growth of deformation bands into echelon and ladder geometries. *Geophysical Research Letters*, **30**, 2033.

Schultz, R.A. & Fossen, H. 2002. Displacement–length scaling in three dimensions: the importance of aspect ratio and application to deformation bands. *Journal of Structural Geology*, **24**, 1389–1411.

Scott, R.B., Harding, A.E. & Hood, W.C. *et al.* 2001. *Geologic Map of Colorado National Monument and Adjacent Areas, Mesa County, Colorado*. US Geological Survey Geologic Investigations Series, Map, **Map I-2740**.

Shipton, Z.K. & Cowie, P.A. 2001. Damage zone and slip-surface evolution over μm to km scales in high-porosity Navajo sandstone, Utah. *Journal of Structural Geology*, **23**, 1825–1844.

Shipton, Z.K. & Cowie, P.A. 2003. A conceptual model for the origin of fault damage zone structures in high-porosity sandstone. *Journal of Structural Geology*, **25**, 333–344.

Shipton, Z.K., Evans, J.P., Robeson, K.R., Forster, C.B. & Snelgrove, S. 2002. Structural heterogeneity and permeability in faulted eolian sandstone: implications for subsurface modeling of faults. *AAPG Bulletin*, **86**, 863–883.

Sibson, R.H. 1996. Structural permeability of fluid-driven fault-fracture meshes. *Journal of Structural Geology*, **18**, 1031–1042.

Sigda, J.M. & Wilson, J.L. 2003. Are faults preferential flow paths through semiarid and arid vadose zones? *Water Resources Research*, **39**, 1225.

Stearns, D.W. 1968. Fracture as a mechanism of flow in naturally deformed rocks. *In:* Baer, A.J. & Norris, D.K. (eds) *Proceedings, Conference on Research in Tectonics (Kink Bands and Brittle Deformation)*. Geological Survey of Canada Papers, **68-52**, 79–95.

Stearns, D.W. & Jamison, W.R. 1977. Deformation of sandstones over basement uplifts, Colorado National Monument. *In:* Veal, H.K. (ed.) *Exploration Frontiers of the Central and Southern Rockies*. Rocky Mountain Association of Geologists, Town, 31–39.

Stone, D.S. 1977. Tectonic history of the Uncompahgre fold. *In:* Veal, H.K. (ed.) *Exploration Frontiers of the Central and Southern Rockies*. Rocky Mountain Association of Geologists, Town, 23–30.

Timoshenko, S.P. & Goodier, J.N. 1970. *Theory of Elasticity*. McGraw–Hill, New York.

Tripp, G.I. & Vearncombe, J.R. 2004. Fault/fracture density and mineralization: a contouring method for targeting in gold exploration. *Journal of Structural Geology*, **26**, 1087–1108.

Vajdova, V., Baud, P. & Wong, T.-f. 2004. Compaction, dilatancy, and failure in porous carbonate rocks. *Journal of Geophysical Research*, **109**, B05204.

Wong, T.-f., David, C. & Zhu, W. 1997. The transition from brittle faulting to cataclastic flow in porous sandstones: mechanical deformation. *Journal of Geophysical Research*, **102**, 3009–3025.

Wong, T.-f., David, c. & Menéndez, B. 2004. Mechanical compaction. *In:* Guéguen, Y. & Boutéca, M. (eds) *Mechanics of Fluid-saturated Rocks*. Elsevier, Amsterdam, 55–114.

Zhao, G. & Johnson, A.M. 1991. Sequential and incremental formation of conjugate faults. *Journal of Structural Geology*, **13**, 887–896.

Received 18 November 2004; revised typescript accepted 21 February 2005.
Scientific editing by Tim Needham